Published in final edited form as:
J Synchrotron Radiat. 2006 January ; 13(Pt 1): 30–45. doi:10.1107/S0909049505036721.

The Structural Biology Center 19ID undulator beamline: facility specifications and protein crystallographic results

Gerd Rosenbaum[a,b], **Randy W. Alkire**[a], **Gwyndaf Evans**[a,‡], **Frank J. Rotella**[a], **Krzystof Lazarski**[a], **Rong-Guang Zhang**[a], **Stephan L. Ginell**[a], **Norma Duke**[a], **Istvan Naday**[c], **Jack Lazarz**[a], **Michael J. Molitsky**[a], **Lisa Keefe**[a,¶], **John Gonczy**[a,b], **Larry Rock**[d], **Ruslan Sanishvili**[a,§], **Martin A. Walsh**[a,‡‡], **Edwin Westbrook**[a,¶¶], and **Andrzej Joachimiak**[a,e,*]

a *Structural Biology Center, Biosciences Division, Argonne National Laboratory, Argonne, IL 60439, USA*

b *SER-CAT, Department of Biochemistry and Molecular Biology, University of Georgia, Athens, GA 30602, USA*

c *Electronics and Computing Technologies, Argonne National Laboratory, Argonne, IL 60439, USA*

d *LR Design, Scottsdale, AZ 85260, USA*

e *The University of Chicago, Chicago, IL 60637, USA*

Abstract

The 19ID undulator beamline of the Structure Biology Center has been designed and built to take full advantage of the high flux, brilliance and quality of X-ray beams delivered by the Advanced Photon Source. The beamline optics are capable of delivering monochromatic X-rays with photon energies from 3.5 to 20 keV (3.5–0.6 Å wavelength) with fluxes up to 8–18 × 10^{12} photons s^{-1} (depending on photon energy) onto cryogenically cooled crystal samples. The size of the beam (full width at half-maximum) at the sample position can be varied from 2.2 mm × 1.0 mm (horizontal × vertical, unfocused) to 0.083 mm × 0.020 mm in its fully focused configuration. Specimen-to-detector distances of between 100 mm and 1500 mm can be used. The high flexibility, inherent in the design of the optics, coupled with a κ-geometry goniometer and beamline control software allows optimal strategies to be adopted in protein crystallographic experiments, thus maximizing the chances of their success. A large-area mosaic 3 × 3 CCD detector allows high-quality diffraction data to be measured rapidly to the crystal diffraction limits. The beamline layout and the X-ray optical and endstation components are described in detail, and the results of representative crystallographic experiments are presented.

Keywords

X-ray beamline; protein crystallography; MAD/SAD; X-ray optics

* E-mail: andrzejj@anl.gov.
‡ Present address: Diamond Light Source, Rutherford Appleton Laboratory, Chilton OX11 0QX, UK.
¶ Present address: IMCA-CAT, University of Chicago, Chicago, IL 60637, USA.
§ Present address: GM/CA-CAT, Biosciences Division, Argonne National Laboratory, Argonne, IL 60439, USA.
‡‡ Present address: Medical Research Council (MRC), ESRF, Grenoble, France.
¶¶ Present address: Molecular Biology Consortium (MBC), Advanced Light Source, Berkeley, CA, USA.

1. Introduction

The Structural Biology Center (SBC) (Rosenbaum & Westbrook, 1997*a*) at Argonne National Laboratory was established by the Department of Energy as a national user facility to serve the expanding and highly demanding macromolecular crystallography community. The SBC was intended to provide highly efficient and flexible X-ray beamlines capable of not only dealing with the very large volume of crystallographic projects but also of satisfying the requirements of the most challenging and diverse crystallographic experiments. The former would be expected to emerge in coming years as a result of major initiatives such as the Protein Structure Initiative (structural genomics) and related initiatives in the wake of the Human Genome Project. Examples of the latter are crystals with very large unit cells (viruses, macromolecular assemblies), very small crystals (microcrystals) and very weakly diffracting crystals (ribosome and other macro-molecular assemblies). In addition, the beamline design and instrumentation was intended to meet the demanding criteria laid down by crystallographic techniques such as multi-and single-wavelength anomalous diffraction (MAD/SAD) (Hendrickson, 1985, 1991) and direct methods applied to macromolecules (Sheldrick, 1998; Weeks & Miller, 1999). Finally, the design called for open access to the sample area to improve crystal mounting, positioning and visualization and for the appropriate space to prepare samples for cryofreezing.

The SBC collaborative access team operates sector 19 of the Advanced Photon Source (APS) (Moncton *et al.*, 1989). The sector consists of two beamlines: bending magnet (19BM) and undulator insertion device (19ID). Both beamlines were essentially built in parallel; however, 19ID was completed first. We present here a description of the ID beamline design, X-ray optics, experimental station configuration, properties of the delivered beam, beamline control software, operational aspects, and selected crystallographic results.

2. Beamline design

2.1. Introduction

Most users care mainly about the endstation with its crystallographic instrumentation and take the delivered X-ray beam as given. However, the source characteristics, the beamline layout and the choice and characteristics of the optical components are very important since they determine the quality of the delivered beam, the operational envelope and ease of operation.

We will describe first the properties of the APS storage ring which is the foundation for the choice of insertion device, then the characteristics of the chosen insertion device, followed by the design considerations for the beamline and the resulting layout, and finally describe the optical components selected and designed to achieve the design goals.

2.2. APS storage ring

The APS storage ring runs at an electron energy of 7 GeV with a nominal average current of 100 mA in its top-up operating mode. It was specifically designed for insertion devices as the predominant X-ray source and a straight section per sector for insertion devices was designed in. Electrons circulating in the storage ring are compressed into bunches and, thus, the generated radiation is emitted in pulses. However, since the bunch frequency is greater than 6 MHz, the source can be considered continuous for all crystallographic applications except sub-microsecond time-resolved experiments. The emittance and other parameters of the storage ring which determine the size and angular width of the electron beam at the site of the insertion device have been improved from the initial high-emittance lattice at the time of the design of the beamline through the commissioning phase to the current lower-emittance lattice (Dejus *et al.*, 2002; http://www.aps.anl.gov/asd/oag/beamParameters.html). In this mode, in which

the storage ring is operated most of the time, the size of the electron beam at the location of the insertion device is 0.65 mm × 0.020 mm [full width at half-maximum (FWHM), horizontal (h) × vertical (v)] and the divergences are 27 μrad × 7 μrad (FWHM, h × v).

2.3. Choice of insertion device

The high electron energy combined with the low emittance of the APS storage ring made undulators the ideal choice as the insertion device for macromolecular crystallography compared with the alternative, wigglers. Undulators funnel all radiation energy spatially into a very narrow cone and spectrally into a few fairly narrow peaks, *i.e.* they have a much higher brilliance than wigglers. This makes undulators far superior for applications where small sample sizes combined with large unit-cell dimensions, *i.e.* large specimen–detector distances, demand the highest brilliance and not just high fluxes. As a result, radiation from the undulator source can better accommodate crystallography projects that require both high flux and high-brilliance X-ray beams. The peaks of the undulator emission, which are a few tens of eV wide, can be shifted over a fairly wide range of photon energy by changing the gap between the magnet structures. At the APS, each sector has direct control of the gap of its undulator.

Undulators at high-energy storage rings produce extremely high power densities in the center of the narrow cone of radiation while the total power is moderate, as opposed to wigglers which produce much lower power densities but very high total power. The high power density impinging on the first crystal of the monochromator will severely degrade its performance if not properly cooled. It was only a year after the start of designing the SBC that calculation showed (Knapp *et al.*, 1994), and subsequent experiments verified (Rogers *et al.*, 1996), that the technique, pioneered at the European Synchrotron Radiation Facility (Buttner, 1993), of cooling the Si crystal of the monochromator to liquid-nitrogen temperature was able to handle the higher power density at the APS. This allowed monochromator designs, including all focusing options, based on proven monochromators at second-generation sources, *e.g.* the National Synchrotron Light Source (Rosenbaum *et al.*, 1988), which are operationally much easier to handle, rather than on the inclined crystal geometry design (Khounsary, 1992) with liquid-gallium cooling (Smither *et al.*, 1989) developed earlier at the APS.

Of the undulator types offered by APS at the time of designing the SBC, undulator A was chosen because its tuning range of 3.5–13.7 keV (3.5–0.9 Å) for the first emission peak, 10–30 keV (1.2–0.4 Å) for the third harmonic and 17–50 keV (0.73–0.25 Å) for the fifth harmonic (Ilinski *et al.*, 1996; Dejus *et al.*, 2002) covered the energy range of interest for macro-molecular crystallography well, including *K*, L_{III} and *M* absorption edges of most elements used for MAD/SAD data acquisition. Also, the convenient overlap between first and third harmonics provides for a wide margin for switching between harmonics, making beamline operation easier. Of particular advantage is that for the most used wavelength, around 1 Å, undulator A, in first harmonic, generates a low heat load on the monochromator while still producing a high X-ray flux near the selenium *K* edge that is used very frequently in protein MAD/SAD analysis.

The effective source size of the photon beam emitted by the undulator is practically identical to the size of the electron beam in the undulator whereas the divergences are slightly larger depending on wavelength. For 12 keV (1.03 Å) in first harmonic, they are 34 μrad × 22 μrad; for 12 keV in third harmonic, 34 μrad × 25 μrad; for 6 keV (2.07 Å), 42 μrad × 31 μrad; and for 18 keV (0.69 Å), 31 μrad × 21 μrad (FWHM, h × v). The angular flux density in the center of the cone is 4–9 × 10^{17} photons s^{-1} $mrad^{-2}$ (0.1% bandwidth)$^{-1}$ (100 mA)$^{-1}$ for photon energies between 3.5 and 20 keV.

2.4. Optical layout

Although fairly narrow in bandwidth, the undulator emission cannot be used directly for macromolecular crystallography. A monochromator is still needed to reduce the bandwidth and to reject all of the emission spectrum except the band centered at the selected photon energy. High monochromaticity ($\Delta E/E \cong 10^{-4}$) is important for MAD data collection. Since the crystals used for monochromatizing X-rays also pass certain multiples of the selected fundamental photon energy, a device acting as a low-pass filter, typically a mirror, is also needed. Besides these functions, the X-ray optics should collect the maximum of the emitted radiation and converge it on the sample in a manner that is optimal for macromolecular crystallographic data acquisition with very small samples and large unit cells.

The horizontal source size of the APS of 650 μm FWHM is much larger than the 50–150 μm size of most samples measured at 19ID. A large horizontal demagnification of the source is desirable in order to focus most of the flux onto small-to-medium size samples. For bending-magnet sources and wiggler sources, the gain in flux density with increasing demagnification is offset by the reduction in acceptance of horizontal divergence from the source as soon as the maximum usable convergence angle on the sample is reached. For the very small divergences of the beam emitted by the undulator, this limitation is practically non-existent even for demagnifications as high as 10:1.

The vertical source size is only 20 μm FWHM, therefore the demagnification is not an issue. However, it is advantageous to limit the distance of the vertically focusing mirror from the sample to 10 m because otherwise the residual surface figure errors of the mirror of the order of 1 μrad r.m.s. would start to dominate and blow up the beam size at the sample. Another important requirement is that the mirror is located downstream of the monochromator so that it is illuminated by the monochromatic beam and does not distort under the intense heat load of the white beam and, therefore, does not need to be cooled. This is an important simplification and cost saving.

We have chosen to sagittally bend the second monochromator crystal as the means to focus the beam in the horizontal direction. Prior experience (Rosenbaum *et al.*, 1992) has shown that a sagittally focusing crystal monochromator produces a very clean aberration-free focus. The disadvantage of the focal length changing with a change of the monochromator Bragg angle, *i.e.* photon energy, can be overcome *via* parameterization or look-up tables. In addition, with the very small divergence of the undulator beam, the depth of field is large and refocusing is only necessary for large energy moves, and is not needed for the different energies used in a MAD-phasing experiment.

The combination of a sagittally focusing monochromator and a vertically focusing mirror provides flexibility of independent focusing in the horizontal and vertical directions on the sample, or on the detector, or to tailor the size of the beam at the sample to whatever is optimal for the experiments.

With the boundary conditions set by available real estate, required walk ways and escape routes, we arrived at a layout that places the monochromator at 54.9 m from the source (center of undulator), the mirror at 57.2 m, and the sample at 62.3 m. The demagnification in the horizontal plane is 7.7:1 when focused on the sample. The (calculated) minimum uncollimated beam size at the sample is 85 μm FWHM horizontal and less than 20 μm FWHM vertical. Smaller beam sizes can be achieved by collimation.

Space has been reserved upstream of the monochromator for additional optical components that may be needed in the future.

3. X-ray optics and beam monitors

3.1. Overview

Most optical elements are located within a radiation shielding enclosure (optics hutch) which extends from 49 m to 60 m from the source. The first active element in the beam is a primary aperture mask at 51.8 m. Next is the monochromator at 54.9 m, followed by the vertical focusing mirror at 57.2 m. Horizontally defining collimator slits are located at 58.9 m, and the vertically defining at 60.2 m (inside the experiment hutch). The last element in the optics hutch is the photon shutter at 59.3 m. The whole beam path, from the front-end connection to the storage ring down to a Be window in the experiment hutch, is under high vacuum with the beam transport pipes enclosed in radiation shielding. The monochromator instrument and the mirror system are housed in large vacuum tanks. The supports for all in-vacuum optical components are separate from the vacuum tanks and are fed into the vacuum *via* bellows. This isolates the optics from vibrations and motions of the vacuum structures under the large atmospheric forces when evacuated. All motions of the optical components and their supports, inside and outside of the vacuum, are performed by encoded DC servomotors, which are remotely controlled.

3.2. Primary aperture mask

The primary aperture is a copper mask with a 4.2 mm × 2.1 mm (h × v) rectangular opening. Its purpose is to remove the bulk of the broad power distribution of the undulator emission and to pass only the narrow cone of the X-ray beam of interest. The aperture is water-cooled and able to absorb up to 8.5 kW, the maximum incident beam power for 300 mA in the storage ring (APS design current). The primary aperture is mounted on top of an *xy* positioning table, which allows the aperture to be centered to the beam. The temperature of the upper, lower, inboard and outboard inside surfaces of the tapered throat of the mask is independently monitored by thermocouples (Rosenbaum & Fornek, 1997). This provides an X-ray beam-position sensitivity of about 50 μm (~1 μrad) with a time constant of a few seconds, making it an excellent beam-position monitor and useful during commissioning as well as operations. The aperture was designed, at the time of the high-emittance lattice, to pass more than 80% of the flux from the undulator in the 5–13 keV range and about 60% between 13 and 25 keV. With the current low-emittance lattice these numbers are 95% and 80%, respectively.

3.3. Monochromator

The monochromator is a double-crystal design with constant height and direction of the monochromatic output beam and a sagittally bent second crystal for horizontally focusing. Using a silicon crystal in 111 orientation, the design allows access to photon energies between 3.5 and 20 keV. However, it is typically operated at energies between 6.0 and 19.5 keV.

The high power density of the undulator would create intolerable distortions in a silicon crystal at room temperature. However, at 120 K, silicon has zero thermal expansion and high thermal conductivity. This reduces the ‘thermal bump’ to a negligible amount (Knapp *et al.*, 1994). The desirable temperature of 100–120 K is achieved by cooling with liquid nitrogen (LN_2). We have developed a direct cooling design with fins of the crystal being immersed in the LN_2 stream and a robust sealing geometry that does not strain the diffracting surface (Ivanov *et al.*, 2000). The first and second crystal are mounted on a common shaft for Bragg-angle control. This shaft extends to a high-precision rotary table (model 1230-P, Moore Special Tool, Brigdgeport, CT, USA) outside of the vacuum tank *via* a frictionless rotary feedthrough [model HS-1500-CF, Ferrotec, Nashua, NH, USA]. The rotary table has a measured reproducibility of 0.1 arcsec, corresponding to 0.04 eV at 12 keV, and an accuracy of 2 arcsec over the range of Bragg angles. The motor control has a resolution of 5×10^{-6} degrees, corresponding to 0.006 eV.

Misalignment between the lattice planes of the first and second crystals in the direction orthogonal to the beam, owing to limited accuracy of the crystal cuts and mechanical tolerances of the mounts, requires a small rotation capability orthogonal to the Bragg rotation (χ rotation) on one of the crystals. χ rotation of the first crystal was easier to implement than on the second crystal bending stage. We chose downward reflection of the first crystal so that the second crystal stage would not be hanging down, making insertion of the second crystal into the bender easier.

The second crystal is held in a bending press applying equal moments at its lateral ends. The bending press consists of a pair of bars above the crystal and a pair of bars being pushed against the crystal from below. The distance between the lower bars is 20 mm larger compared with the upper bars. The upper bars define the angular orientation of the crystal. The applied bending moments generate the cylindrical shape (cylinder axis parallel to the beam, sagittal bending) required for horizontal focusing. The bending moment is motor controlled. The actual bending area of the crystal is a 10 mm-wide section in the middle thinned to 0.64 mm. The 'wings' of the crystal are 4–10 mm thick and essentially do not bend. At a ratio of 7.6 of length (in beam direction) over width of the bent section, anti-clastic bending, which generates a small gradient to the Bragg angle along the footprint of the beam, is negligible. For maximizing the flux, the Bragg angle of the second crystal must be precisely matched to that of the first crystal. In addition, the capability to remove any twist is essential for a bent crystal. To that end, each bending couple can be rotated around a horizontal axis orthogonal to the beam. For Bragg-angle 'tuning', the motors at each bending couple are moved in the same direction. For de-twisting, the motors are moved in the opposite direction. The resolution of these motors is about 50 nm.

The bender assembly is mounted on a translation stage controlling the distance (orthogonal to the lattice planes) between the first and second crystals for constant height of the exit beam. This stage in turn is mounted on a stage translating the second crystal parallel to its lattice planes such that it intercepts the beam reflected from the first crystal in its center.

A substantial fraction of the radiation incident on the first crystal is scattered. If part of the scattered radiation is absorbed by the mechanics of the second crystal, small distortions result and the Bragg-angle tune for maximum flux is lost. The small beam size allows the first crystal to be very tightly surrounded with shielding. The temperature of the scatter shield is a balance of heat absorbed from the scattered radiation and heat lost to the first crystal assembly at LN_2 temperature. Thermal stabilization by water cooling is necessary. The second crystal is also thermally stabilized at 298 K using a copper braid from a water-cooled block to the trolley containing the focusing mechanism. The difference in temperature between the first and second monochromator crystals implies that the monochromator operates in a slightly dispersive mode. The effect of this dispersiveness can be calculated and compensated by small adjustments to the distance between the crystals and, in angle, by small adjustments to the angle of the vertically focusing mirror (see below) to keep the beam to the sample at constant height and angle. For small energy changes, as occur during MAD data acquisition, the dispersive effects are negligible.

The time required to change energy has two components: first, the time to change the Bragg angle including decay of any vibrations, and second, the time for thermal equilibration after a related change of the undulator gap. The change of Bragg angle plus vibration decay takes only a few seconds. The time for thermal equilibration depends entirely on the extent of the heat-load change from the undulator. Even though the scatter shield is cooled, the temperature of the scatter shield can change dramatically, *e.g.* rise by 70 K when going from 12 keV in the first undulator harmonic to 19 keV in the third harmonic. A small part of the scattered radiation and the thermal radiation from the scatter shield reach the second crystal and its mounting

hardware. This can cause extended thermal equilibration times. However, for the most-used energy range between 7 and 13 keV with the undulator in first harmonic, the change of heat load is small and little equilibration time is needed (see §7)

3.4. Vertically focusing mirror

The mirror substrate is a 1.02 m-long and 100 mm-wide flat made of ULE (ultra-low-expansion titanium silicate) and manufactured by Insync (Albuquerque, NM, USA). It has a measured surface roughness of 2.0 Å r.m.s. and a 0.7 μrad r.m.s. surface figure error. The mirror is downward reflecting and fully adjustable in terms of height, angle and radius of curvature. Downward reflection was chosen for easier access to the bender mechanics and for preventing dust settling on the active surface when the lid on the top of the tank is opened. The height and angle drives are outside of the mirror tank and feed into the vacuum *via* bellows. The bending mechanism for focusing is inside the vacuum tank. Motor-driven lever arms attached to each end of the mirror generate the required bending moment. The motors may be driven in synchrony for a cylindrical bend or independently to approximate an elliptical figure of the mirror surface for reduction of spherical aberrations. The mirror surface is divided into three tracks parallel to its long side. The central track has no coating and the two outer tracks are coated with platinum and palladium, respectively. At the normal settings of 2.5 mrad grazing incidence, the uncoated track is used for photon energies below 14 keV, the Pd-coated track for 14–24 keV and the Pt-coated track should energies above 24 keV be desired (using the Si 333 reflection). These settings provide safe rejection of higher-order harmonics (0.036%). A lateral translation of the whole mirror assembly inside the vacuum tank allows the appropriate track to be moved into the beam. This way, the specified energy range can be covered without changing the mirror angle and, thus, without changing the beam height at the slits or sample goniometer.

3.5. Slits

Two sets of computer-controlled tungsten slits are installed on the beamline, each having a vertically defining and a horizontally defining pair of blades: the first set is located midway between the optics and sample (‘Horizontal Collimator Slits’ and ‘Vertical Collimator Slits’ in Fig. 1), and the second set is located 210 mm upstream of the sample (Fig. 2, §4.3). For regular operations, the first slits are open and only the second set of slits are used to collimate the beam dimensions to the size of the crystal. When very low-angle data need to be measured, a configuration routinely used for small-angle scattering is implemented using the upstream set of slits to collimate the beam, and using the second set of slits close to the sample as guard slits blocking the very low-angle scatter generated by the blades of the collimating slits. The blades of the first set can be moved as a pair and one of the blades can be moved individually for size control.

3.6. Photon shutter

The photon shutter consists of two tungsten blocks of length 65 mm that can be inserted by pneumatic actuators into the monochromatic beam path. Positioned close to the downstream wall of the optics radiation enclosure, they also seal off the enclosure in terms of radiation safety. This allows the experimenter to enter the experiment hutch without closing the main radiation shutter in the front end, thus keeping the optics under steady heat load. The photon shutter is part of the personnel safety system.

3.7. Personnel safety system

The personnel safety system is an electronic interlock system (mandated, installed and maintained by APS) that prevents people from being exposed to radiation. Radiation shutters

can only be opened after downstream radiation enclosures have been searched, closed and locked, and safe conditions, *e.g.* coolant flow, for critical components have been established.

3.8. Beam-position monitor

In order to keep the X-ray beam focused onto the slits, precise beam positioning is necessary. To meet this need, a novel beam-position monitor (BPM) has been developed (Alkire *et al.*, 2000), based on a design used as an intensity monitor (Alkire & Rotella, 1997). The BPM consists of an array of four PIN diodes located upstream of a 0.5 μm-thick metal foil placed in the X-ray beam. X-rays absorbed by the metal foil generate fluorescence radiation, which is then detected by the diode array. The solid angle of fluorescence picked up by each diode is a function of beam position relative to the array. Dividing the difference of the diode signals by the sum for vertical and horizontal pairs, two-dimensional position information is obtained. The device is vacuum compatible, has a tracking range of 8 mm × 10 mm and a measured position sensitivity of 1–2 μm.

Three BPMs are currently installed on the 19ID beamline. The first is located immediately downstream of the monochromator, the second upstream of the exposure timing shutter (see §4.2) and the third immediately downstream of the second slit set (Fig. 2). The second BPM is used primarily to set the tune of the second crystal, but can also be used for examining the twist of the second crystal (Alkire, Duke & Rotella, 2004). Feedback from the second BPM to the monochromator tune is currently being developed (Lazarski *et al.*, 2004) to correct for tune drift. However, since development of top-up operating mode at the APS, X-ray ring current decays by only a few percent before re-injection every 2–4 min. This stabilizes the heat load on the monochromator and reduces beam drift to not more than a few microradians per day, requiring only occasional attention by the user. The location of this BPM upstream of the timing shutter allows tuning with this shutter closed, minimizing sample exposure to X-rays. The third BPM is available as an alignment aid when the second slit set is open, but its primary function is to monitor reference intensity after the slits have been adjusted to their operational sizes.

4. Experiment station

4.1. Overview

All components of the experiment station (Fig. 2) are contained within a radiation shielding enclosure (experiment hutch) which extends from 60 m to 67 m from the source. It has been designed to be large enough to accommodate the equipment necessary for routine crystallographic measurements, as well as any additional apparatus needed for special experiments.

The components are (in sequence along the beam): the vertical collimator slits at 60.2 m, the beryllium window at 60.4 m, the second BPM at 60.9 m, three filter shutter arrays in series at 61.3–61.6 m, the second slits (the actual collimator slits) at 62.1 m, the κ goniometer at 62.3 m (sample position), and the detector at 0.1–1.5 m downstream of the sample. The high-vacuum system ends at the Be window. From there on to the exit from the guard slits, the beam is traveling in a rough vacuum (~0.2 torr) to eliminate scatter and absorption.

Other components are the sample alignment microscopes, the sample cryocooler, the fluorescence detector and the detector support system (A-frame). Fig. 3 shows a close-up view of the κ goniometer and the sample environment. Fig. 4 gives a wider view of the experimental area with the detector support and the detector moved away from the sample for easier sample mounting.

4.2. Filter/shutter assembly

The X-ray timing shutter is a critical component of the beamline that can strongly affect data quality. In the initial design a filter/shutter unit from XIA (X-ray Instrumentation Associates, Newark, CA, USA) has been used for exposure timing. Two of the four pneumatically driven blades were used as the shutter, the other two carry filters. A second identical unit served as back-up shutter. A third unit has only filters. The pneumatic valves for the shutters were activated from an electronic module that receives timing signals from the control electronics of the sample goniometer for precise synchronization of the exposure with the rotation interval of the goniometer. The jitter of the delay between the electronic signal and the actual beam closing or opening was less than ±0.5 ms initially. However, over time the timing of this shutter became inconsistent. Recently, the XIA shutter has been replaced by a Uniblitz shutter (model XRS6, Vincent Associates, Rochester, NY, USA) mounted on the downstream end of the guard slit housing. The jitter of the delay of this shutter is less than ±0.1 ms and it does not show any aging, with more than one million shutter cycles per year.

A set of aluminium and silver foils of varying thickness are installed in the filter arrays and can be used to attenuate the X-ray beam to prevent saturation of the detector. The materials, thicknesses and number of filters were chosen to provide reasonably fine stepped attenuation over the entire energy range accessible at the 19ID beamline. The attenuation factor is selected from a graphical use interface and an appropriate set of foils are inserted into the beam automatically.

4.3. Slit assembly

The second slit set assembly is used for collimating the beam to the optimal size for the experiment. It consists of four individually adjustable blades housed in a vacuum-tight box. The blades are made of tungsten. Their knife edges are polished to minimize scatter. A third BPM is integrated into the slit box immediately downstream of the slits. When the slits are set, it serves as an I_0 monitor. A Kapton window on the downstream end of the box terminates the rough vacuum section. From there, the X-ray beam passes through the Uniblitz timing shutter and then through a tube that ends 15 mm upstream of the sample. A removable plug with a 0.5 mm-diameter hole is inserted into the downstream end of the tube and serves as a scatter guard. The whole X-ray beam path from the Kapton window to the open plug is flushed with helium to minimize scatter.

The slit box is mounted on an *xy* translation stage. For alignment, the box is first moved as to center the hole in the scatter guard plug to the X-ray beam, then the slits are individually centered to the beam. Once centered, they can be symmetrically adjusted to the desired size to set the X-ray beam size (typically within the range 20–300 μm). Since the centering of the blades is relative to the opening in the plug, this is a one-time alignment. From then on, only the whole assembly needs to be aligned to the beam.

4.4. *κ* goniometer

In order to provide full flexibility in orienting crystal samples for optimal data acquisition strategies we have designed a miniature *κ* goniometer (Rosenbaum & Westbrook, 1997*b*). The *κ* stage is mounted on an industrial high-precision rotary table (model 1230-S, Moore Special Tool) which provides the ω rotation. The angle between the *κ* and ω axes is 60°. The ϕ stage is mounted on a linear translation stage (*z*-translation), which is mounted on the *κ* arm. At zero *κ* angle, the ϕ axis is collinear with the ω axis. The *z*-translation, which is collinear with the ϕ axis, accommodates a wide range of lengths of sample mounting pins. For manual sample centering, a small *xy* translation stage is attached to the head of the ϕ shaft. Magnets suitable in size for the different pin types that users bring to the beamline can be mounted on the *xy* stage.

For alignment of the center of the goniometer to the center of the X-ray beam, the entire κ goniometer is mounted on an *xy* positioning platform with better than 0.5 μm resolution. The ω axis has a measured eccentricity of better than 5 μm. The 'sphere of confusion' of the sample, when rotated with the ω axis only, which is the most common mode of data acquisition, is about 10 μm in diameter. For alignment of the κ instrument, first the ϕ stage is finely adjusted in angle until the ϕ axis intersects the κ axis. Then the mount of the κ instrument to the ω table is adjusted so that the intersection point lies on the ω axis. This is then 'the center of the goniometer'. For the combined ω, κ and ϕ rotations, the observed sphere of confusion is about 20 μm in diameter.

The ω table has a maximum speed of 10° s^{-1}, an accuracy of better than 0.002°, a repeatability of better than 0.0002° and a resolution of the motor control of 6×10^{-6} degrees. The κ drive has a speed of 7° s^{-1} and a resolution of 4×10^{-5} degrees. The ϕ drive has a speed of 22° s^{-1} and a resolution of 3×10^{-3} degrees. The *z*-translation has a range of ± 8 mm with a resolution of <0.1 μm. The κ, ϕ and *z*-drives are all backlash free. The *xy* translation stage on the ϕ spindle is the only manual operated stage. Several motorized versions of the *xy* translation stage are being evaluated.

4.5. Beam stop

A composite beam stop, designed and fabricated locally (Alkire, Schuessler *et al.*, 2004), protects the CCD detector (see below) from exposure to the direct X-ray beam. The beam stop was made out of a 100 mm × 12 mm × 1 mm-thick tungsten plate with a 0.5 mm-diameter × 2 mm-deep cavity machined into the end of the plate to intercept the direct beam. Outside the beam-stop cavity the surface of the beam stop is covered with indium metal, blocking tungsten fluorescence from the beam stop surface and emitting only low-energy emissions (~4 keV) from indium if the direct beam hits outside the main cavity. The beam stop is mounted on a support rail, offset in height by 150 mm from the beam-stop cavity. The *xy* translation of the beam stop is motorized. The beam-stop-to-sample distance and beam-stop angle are adjusted manually.

4.6. CCD detector

From the commissioning of the beamline through August 2004, an area detector (SBC2) designed and constructed at Argonne National Laboratory (Westbrook & Naday, 1997) was used. In September 2004, an ADSC Quantum 315 (Q315) detector (Area Detector Systems, Poway, CA, USA) was installed. Both detectors are 3 × 3 mosaic tapered fiber-optic-coupled CCD detectors. SBC2 has an active area of 210 mm × 210 mm, while the active area of Q315 is 315 mm × 315 mm. The larger active area of Q315 with comparable peak resolving power considerably increases the efficiency of data acquisition with respect to completeness and high resolution. Currently the SBC2 detector serves as a back-up detector for 19ID. Both detectors can be operated in 'full mode' where each pixel is read out, or in 'binned mode' where every two adjacent rows and columns are summed before readout. The SBC2 has 3072 × 3072 pixels in full mode (1536 × 1536 effective pixels in binned mode) with a pitch of the pixels, back projected on the detector face, of 68.4 μm (136.7 μm effectively in binned mode). Q315 has 6144 × 6144 pixels in full mode (3072 × 3072 effective pixels in binned mode) with a pitch of the pixels, back projected on the detector face, of 51.3 μm (102.5 μm effectively in binned mode). For many experiments where medium-size unit cell crystals are being measured, the lower-spatial-resolution 2 × 2 binned mode of operation suffices, and the size of the image data files can be reduced from 76 to 19 MB for Q315 (19 to 4.8 MB for SBC2). For very large unit cells or high-resolution data collection the unbinned mode is used. The total time overhead for data readout and transfer to disk of Q315 in binned mode is currently about 2.7 s, and 3.7 s in full mode. The overhead for SBC2 was approximately 3.8 s in unbinned mode and 2.6 s in binned mode.

The resolving power of the SBC2 detector and the beamline was demonstrated (Fig. 5) when diffraction data from the 50S ribosomal subunit (Nissen *et al.*, 2000; see §8.2.1) were acquired and more than 500 diffraction peaks across its 210 mm face were recorded and intensities were successfully processed. It is expected that ~750 diffraction peaks can be resolved on the ADSC detector.

4.7. Sample alignment

The possibility of using a fully focused X-ray beam with dimensions 85 μm × 20 μm (FWHM), that can be reduced *via* slits to ~20 μm × 20 μm, to expose samples with dimensions as small as a few micrometers, creates the need for a very precise and accurate sample positioning system and high-powered sample visualization apparatus. To allow visualization and alignment of small crystals, two high-magnification long-working-distance microscopes with color CCD camera systems are directed at the sample. They are mounted on the goniometer base with their optical axes aligned with the center of the κ goniometer. One camera is looking vertically up. The other camera is above the guard slit box looking with the beam at angle of 30° to the horizontal. Using both cameras, samples can be aligned efficiently in a single step. Typically, alignment is verified by rotating samples in ω while observing their position.

4.8. Sample cryocooler

An Oxford Cryosystems nitrogen-gas cold stream is used to cool protein crystals to ~100 K. The cold stream is mounted from above the sample area, leaving the sample location unobstructed. For sample mounting, the κ angle is moved to −60°, allowing LN_2-filled sample vials to slide directly up to the base magnet. Removal of the vials leaves the sample bathed in the cold stream. If requested, a helium-gas cold stream can be installed to cool protein crystals to ~15 K.

4.9. Fluorescence detector

Optimal energy settings for MAD/SAD experiments are determined by scanning the X-ray energy near the absorption edge of a desired element in the sample and recording the fluorescence emission spectrum. A multi-channel energy analyzer is available through an Amptek model XR-100CR detector (186 eV resolution at 5.9 keV; Amptek, Bedford, MA, USA), allowing the presence of target elements to be detected prior to conducting fluorescence scans. This measurement also alerts the user to the presence of any other fluorescing elements in the sample that may interfere with the measurement (for example, arsenic in the presence of selenium). In such cases adequate measures must be taken to optimize the fluorescence detector energy window. In addition, a Bicron photomultiplier detector (Saint-Gobain Crystals and Detectors, Newbury, OH, USA) can be used for faster fluorescence measurements if high-energy resolution is not needed. Both detectors use Ortec (Ametek, Advanced Measurement Technology, Oak Ridge, TN, USA) electronics to isolate the target element emission energy.

4.10. Detector support

A large overhead A-frame has been designed to support and position the heavy CCD detectors and other instruments. It is completely isolated from the goniometer to prevent any disturbance of the very sensitive sample position when the heavy detector is moved. Also, the overhead support provides free access to the sample area without any support tables or rails to bend or step over. Being a hanging load, the position of the detector is very stable.

A heavy-duty trolley running on rails on top of the A-frame provides horizontal translation along the beam direction. A vertical translation stage is mounted on the trolley. On the initial support for the SBC2 detector, angular positioning was provided by a rotation stage between the vertical translation and the cradle in which the detector was mounted. To accommodate the

much larger and heavier Q315 detector, the rotation stage was replaced for reasons of robustness by a second vertical translation which, when driven in the opposite direction to the first vertical translation, provides rotation of the detector. After initial calibration of the positions of the translation stages for the detector at a reference position, a computer program calculates the coordinates of the *x* and *y* translations for the requested detector-to-sample distance, detector angle relative to the beam (2θ), and offset of the detector center relative to the beam center, taking into account the angle of the beam reflected by the vertically focusing mirror.

The current operational range of the Q315 detector is: sample-to-detector distance from 100 to 1500 mm, vertical offset from 100 mm below to 400 mm above the nominal beam height, and 2θ rotation from −5 to 40°. Since the detector is routinely moved to 800 mm from the sample for sample mounting, the reproducibility of the detector position orthogonal to the beam is critical. This reproducibility has been determined to be better than ±20 μm, which is less than the pixel size in full resolution and small compared with the typical spot size of 350 μm. The reproducibility of the detector-to-specimen distance is also ±20 μm.

5. Measured properties of the X-ray beam

5.1. Methods

Initial characterization of the beamline entailed assessing the focal properties of the optical elements, determining the energy resolution of the monochromator and harmonic contamination of the output beam, and measuring the flux delivered by the optics to the sample. The results are shown in Table 1.

The focal spot size was determined separately for the vertical direction (mirror focus) and the horizontal direction (sagittal focus) by scanning a 13 μm-wide tungsten slit aperture through the focus. The transmitted intensity was recorded using a PIN-diode detector mounted on the slit assembly. The recorded profile was then deconvoluted with the slit size.

The energy resolution of the beamline was determined by mounting a silicon crystal as an analyzer at the sample position and recording a high-order back reflection as a function of incident X-ray energy. The width of the profile of the recorded diffracted intensity was then deconvoluted to account for the energy width of the analyzer crystal itself.

X-ray flux measurements were performed using a dry-nitrogen-filled ionization chamber of active length 100 mm. The recorded current was converted to the rate of incident photons using tabulated mass absorption coefficients of nitrogen (McMaster *et al.*, 1969), assuming standard density, a work function of 34.6 eV per electron–ion pair, and assuming that all energy of the absorbed photons is converted into electron–ion pair production. These assumptions are permissible since there was no need to measure the intensity of the beam to better than 10% accuracy considering that the actual flux intercepted by a sample varies much more depending on a large number of parameters of an individual experiment.

The harmonic contamination of the output beam was determined by inserting aluminium filter foils that attenuate substantially at the fundamental photon energy, but only a small fraction at the higher harmonics passed by the monochromator. Tabulated mass absorption coefficients (McMaster *et al*., 1969) were used to calculate the ratio of attenuation at the harmonics relative to the fundamental photon energy and the ratio of absorption in the ion chamber. In addition, the ion chamber signals with one, two and three identical foils of about 10× attenuation were used to check consistency.

5.2. Energy resolution

The energy resolution of the Si 111 double-crystal monochromator was measured at 12.305 keV with an unfocused beam collimated to a height of 0.1 mm. A silicon crystal in back-reflection mode (*h*,*k*,*l* = 9,5,1) was used as an analyzer. The FWHM of the recorded profile was 1.74 eV which corresponds to an energy resolution of 1.41×10^{-4} ($\Delta E/E$). This is essentially equal to the intrinsic width of the Si (111) reflection calculated theoretically (Matsushita & Hashizume, 1983). The form of the profile is very close to the ideal case predicted by Darwin (1914). This is a strong indication that the LN_2 cooling of the first monochromator crystal is effective in minimizing the effects of the very high power density of the undulator radiation. Indeed, the almost ideal behavior of the system suggests that there is no noticeable distortion of the first monochromator crystal.

5.3. Flux characteristics

The flux at the sample position was measured with the APS operating at 100 mA with the undulator's first harmonic and the Si 111 monochromator set at 12 keV. A value of 1.3×10^{13} photons s^{-1} was measured, corresponding to a flux density of 3.6×10^{15} photons s^{-1} mm^{-2}.

By choosing the focal lengths of the monochromator and mirror, the flux density at the sample position can be varied between ~1×10^{12} and 3×10^{15} photons s^{-1} mm^{-2}. Because of the insignificant harmonic content of the X-ray beam when the mirror is in place (less than 0.036%), further decreasing of flux on the sample can be achieved by use of an array of metal foil attenuators without the risk of enhancing harmonic contamination (beam hardening) significantly.

6. Beamline control, user interface and data acquisition

6.1. Beamline control

The 19ID beamline is controlled from a top-of-the-line workstation running Linux with large dual monitors for convenient display of graphical user interfaces for beamline control, data collection, data processing and structure determination. The beamline is equipped with eight IOCs (input output controllers), four controlling and monitoring the servo motors of the beamline and four controlling and monitoring other beamline hardware, *e.g*. electrometer amplifiers, timing shutter, attenuators and vacuum gate valves. The platforms of the IOCs are embedded computers on a VME bus (Motorola MVME167, CPU 20 MHz, 16 MB RAM) running the real-time operating system *vxWorks* (Tornado II). The software controlling beamline components and running on the IOCs consists of drivers, sequencers and databases using *EPICS* (Experimental Physics and Industrial Control System, http://www.aps.anl.gov/epics). The IOCs are connected to and communicate with each other over an Ethernet network. The core of the software is written in C and SNL (state notation language).

For different types of functions there are different IOC masters, which control other IOCs by executing sequencer programs or by using scan records from *EPICS*. For example, fluorescence scans used in determining optimal energies for MAD/SAD experiments are conducted by executing a scan record from 19idexp; data collection, on the other hand, is controlled from the software IOC (soft IOC) residing on a SunFire SOLARIS Server (see below). Parameters are specified by a user for a particular experiment *via* graphical user interfaces, which pass these parameters to the appropriate IOCs.

6.2. User interface and data acquisition

The main interface used to communicate data-collection parameters to specific IOCs is *SBCcollect. SBCcollect* is a client process that works together with a server process (*SBCserver*) (Lazarski *et al*., 2006; Minor *et al*., 2005). *SBCserver* communicates directly with all beamline IOCs through channel access protocol and TCP sockets. *SBCserver* is written with a 'personality facility', which allows commands to be communicated to *SBCserver* with different syntax from diverse sources, *e.g*. one can act as a watcher only, the other could have full control over a specific experiment. The protocol that is used for communication between clients and *SBCserver* consists of plain-text ASCII commands. Several additional modules of *SBCserver* are being developed to interact with a crystal-mounting robot, *HKL2000* and other devices and clients (Lazarski *et al*., 2006).

SBCcollect is a graphical user interface that allows users to specify particular experiment parameters for data acquisition and then run the experiment *via SBCserver. SBCcollect* continuously monitors the real-time status of all components relevant for the data-acquisition process. It also monitors the progress of data acquisition by continuously displaying diffraction images. Users may interact with these diffraction images in real time or recall images collected previously. *SBCcollect* uses color to bring user attention to specific text fields or buttons. It evaluates all input in an attempt to recognize and prevent operator error, *e.g*. overwriting already collected images, collision of beamline components and disk space availability for writing images. Fig. 6 depicts the main window of the *SBCcollect* interface.

6.3. Data storage and processing

All diffraction data are transferred from the Q315 frame grabber computers to the SunFire Server (eight UltraSparc CPUs, 8 GB RAM, 10 TB fiber channel storage). The transfer is conducted through a 1 Gbps Ethernet private network. From the SunFire Server, data are accessible through one of four SBC subnets dedicated for slower (also 1 Gbps Ethernet) file operation to processing nodes using the NFS (network file system) protocol. Five workstations are available to the active and previous user group each for data reduction. The data-processing workstations are dual-processor fast top-of-the-line PCs running Linux. Beamline 19ID offers to users for data processing all major software suites including *HKL2000* (Otwinowski & Minor, 1997), *MOSFLM* (Leslie, 1999) and *d*TREK* (Pflugrath, 1999).

7. Beamline operation

Users control the operations necessary to set up and design experiments, execute data collection and analyze and process data *via* a graphical user interface. Some operations and special beamline set-ups require staff assistance. Besides sample rotation, *z*-translation, exposure and detector-related functions, users control the wavelength setting of the monochromator and undulator, sample alignment motions, goniometer position, detector positioning and slit sizes.

The facility can accommodate a diverse set of crystal mounting pins as well as capillary mounts. Typically, samples are mounted cryogenically on a magnetic pin base attached to a manually adjusted *xy* support stage. A motorized height adjustment as part of the κ assembly allows any commercially available pin length to be used for sample mounting. For crystal alignment, two high-magnification cameras (see §4.7) are attached to the goniometer base and move with it so that their centers of field-of-view stay precisely aligned to the center of the κ goniometer (intersection of its rotation axes). Adjustable camera magnification allows crystals as small as 5 μm to be seen clearly. Cross-hair box overlays in the displays mark the beam area as target for the sample alignment. A variety of adjustable sample illuminators have been implemented to meet user needs. External fiber-optic light sources shine on the crystal as well as on a pneumatically driven (Teflon) reflector attached to the cold-stream nozzle. The reflector

creates backlighting directly along the camera optical axis, greatly enhancing sample contrast. By placing a fluorescent screen at the sample position, users can verify, and correct if necessary, the centering of the goniometer to the beam.

Typically, energy changes around the absorption edges of most elements are performed by the user, but large energy changes require staff assistance. This also includes fluorescence scanning for MAD/SAD experiments.

For first-order harmonic radiation above 7 keV, the undulator is relatively wide open. Changing energy is, therefore, mainly dependent upon optimizing the tune of the second crystal and aligning the beam onto the sample position, a process requiring only a few minutes. For energies below 7 keV in first-order harmonics mode, some equilibration time is necessary due to Compton heating of the components inside the monochromator. Heat loads increase significantly beyond 13.5 keV when the third harmonic of the undulator has to be used requiring the undulator gap to be closed. Combined with the narrower Bragg width at higher photon energies, it can lead to equilibration times in excess of 1 h before the monochromator is fully thermally stabilized. At 19 keVand 100 mA, for example, Compton shielding temperatures can rise by 70 K compared with 12 keV in the first-order harmonic. This equilibration time is required for the initial change and must be allowed for when returning to reduced heat-load conditions.

If the full flux of the X-ray beam were focused on the sample, exposure times would have to be limited to 20–50 ms to avoid saturation of the detector. Considering the current overhead of detector readout and data transfer, exposure times of less than 1 s would not improve the overall speed of data collection. Very short exposures are also not recommended because some millisecond beam fluctuations and instabilities may introduce errors. For this reason the beam size at the collimating slits 210 mm upstream of the sample is adjusted to 350 μm × 350 μm by focusing at 12 keV about 800 mm downstream of the sample. This produces a spot size on the CCD detector that is less than the slit size at all sample-to-detector distances and still maintains a high photon flux on the sample (1×10^{12} photons s^{-1}) using 200 μm × 200 μm slits. If higher photon flux is needed then a look-up table, based on a linear interpolation from measured focusing curves, can be used to adjust each focusing optic. Lower flux is accomplished by X-ray beam attenuation with a set of foils.

User operations and the use of beam time can be greatly improved by automation of routine procedures and implementation of robotics (Snell *et al*., 2004; Pohl *et al*., 2004). The SBC facility is in the process of implementing automated protocols for energy change and tune, fluorescence scans, robotic sample mounting (Shu *et al*., 2004) and other applications. These advances, when combined with superior optics, computer resources and highly experienced and dedicated staff, will simplify beamline control, optimize experiments and increase their success rate, therefore leading to better use of valuable beam time. A diverse set of crystallographic software suites are available to users and interactive stereographics are provided for users allowing structure determination on site.

8. Crystallographic performance

8.1. Performance statistics

From the beginning, the 19ID beamline has been in the forefront of all synchrotron beamlines. Since 2001, 19ID has been established as the most productive facility in macro-molecular crystallography. In 2004 a record 176 PDB (Protein Data Bank) deposits resulted from data collected at beamline 19ID and currently data collected at 19ID accounts for 646 structures in the PDB (Fig. 7). Moreover, the average structure size is the largest at the APS and 19ID has been applied to the most challenging projects in macromolecular crystallography.

8.2. Examples of structures solved with data acquired at 19ID

Below we give examples demonstrating the wide range of demanding structures that have been solved using data acquired at 19ID, from extremely large structures to ultra-high resolution, to extremely large unit-cell sizes, and to MAD phasing in the presence of a large number of anomalous sites. These exemplary experiments attest to the flexibility and performance of the beamline.

8.2.1. Ribosome—The structure of the ribosome, a basic component of protein synthesis machinery in every cell, has been pursued for over 20 years. Several groups have taken advantage of the 19ID capabilities and determined crystal structures of 50S and 30S ribosomal subunits. The large ribosomal subunit catalyzes peptide bond formation and binds initiation, termination and elongation factors. The crystal structures of 50S ribosomal subunit from *Haloarcula marismortui* and *Deinococcus radiodurans* were determined at high resolution using data collected at beamline 19ID (Ban *et al*., 2000; Schluenzen *et al*., 2001). The structures include RNA, proteins and inhibitors. The domains of its RNAs all have irregular shapes and fit together in the ribosome like the pieces of a three-dimensional jigsaw puzzle to form a large monolithic structure. Proteins are abundant everywhere on its surface except in the active site where peptide bond formation occurs and where it contacts the small subunit. Most of the proteins stabilize the structure by interacting with several RNA domains, often using idiosyncratically folded extensions that reach into the interior of the subunit.

The small 30S ribosomal subunit performs the decoding of genetic information during translation. Two crystal structures of the 30S ribosomal subunit from *Thermus thermophilus* show the decoding center in functionally activated subunit (Schluenzen *et al*., 2000) and show that the decoding center, which positions messenger RNA and three transfer RNAs, is constructed entirely of RNA (Wimberly *et al*., 2000). The entrance to the messenger RNA channel will encircle the messenger when a latch-like contact closes and contributes to processivity and fidelity. Extended RNA helical elements that run longitudinally through the body transmit structural changes, correlating events at the far end of the particle with the cycle of mRNA translocation at the decoding region. 96% of the nucleotides were traced and the main fold of all proteins was determined. The latter are either peripheral or appear to serve as linkers. Some may assist the directionality of translocation.

Crystal structures of the 30S ribosomal subunit in complex with messenger RNA and cognate transfer RNA in the A site, both in the presence and absence of the antibiotic paromomycin, have been solved (Ogle *et al*., 2001). These structures showed that cognate transfer RNA binding induces global domain movements of the 30S subunit and changes in the conformation of the universally conserved and essential bases of the 16S RNA. The conserved bases of the 16S RNA interact intimately with the minor groove of the first two base pairs between the codon and anticodon, thus sensing Watson–Crick base-pairing geometry and discriminating against near-cognate transfer RNA. The third, or ‘wobble’, position of the codon is free to accommodate certain non-canonical base pairs. The antibiotic paromomycin facilitates binding of near-cognate transfer RNAs by inducing small structural changes.

These fundamental structures of 50S and 30S ribosomal subunits have stimulated extensive structural studies of antibiotics binding to ribosome. These studies were made possible because facilities such as 19ID became available for data collection (Clemons *et al*., 2001).

8.2.2. Aldose reductase—Atomic-resolution studies have been limited to peptides and small proteins. The first subatomic resolution structure of a 36 kDa aldose reductase (AR) was obtained using data collected at 19ID (Howard *et al*., 2004). The structure of the AR complex with its cofactor NADP+ and inhibitor IDD 594, a therapeutic candidate for the treatment of diabetic complications, has been determined at 0.66 Å resolution (Table 2). The very well

ordered model and the electron density maps revealed fine features, such as H atoms, bond densities and significant deviations from standard stereochemistry. Other features, such as networks of hydrogen bonds, a large number of multiple conformations, and solvent structure were also better defined. Most of the atoms in the active-site region were extremely well ordered (mean $B \simeq 3$ Å^2), leading to the identification of the protonation states of the residues involved in catalysis. The electrostatic interactions of the charged carboxylate head of the inhibitor with the catalytic residues and the charged coenzyme NADP+ explained the non-competitive character of the inhibitor. Furthermore, a short contact involving the IDD 594 bromine atom explained the selectivity profile of the inhibitor, an important feature to avoid toxic effects. The presented structure and the details revealed are instrumental for better understanding of the inhibition mechanism of AR by IDD 594 and, hence, for the rational drug design of future inhibitors. This work demonstrates the capabilities of subatomic-resolution experiments and stimulates further developments of methods allowing the use of the full potential of these experiments.

8.2.3. MAD/SAD experiments—The MAD/SAD method has become prominent in solving the phase problem (Hendrickson, 1991; Walsh, Evans *et al*., 1999). In this method, variations in the diffraction pattern arise from the selective absorption of X-rays at given wavelengths. When combined with cryofreezing of protein crystals (Garman, 1999), this method allows a complete multiwavelength data set to be collected from a single crystal. Therefore, the diffracting crystal remains the same, and in principle there is no error due to non-isomorphism. The first structure determined at 19ID using the MAD approach was FHIT protein (Lima *et al*., 1997). Upon further improvements we have shown that, for a small protein, MAD/SAD data can be collected in less then 30 min (Walsh, Evans *et al*., 1999). We have also shown that such an approach can be easily extended to much larger proteins such as cyanase. Cyanase is a homodecamer of 17 kDa subunits. The enzyme crystallizes in the triclinic space group *P*1 with unit-cell dimensions of a = 76.34, b = 81.03, c = 82.30 Å, $\alpha = 70.3°$, $\beta = 72.23°$ and $\gamma = 66.43°$. The asymmetric unit contains one 170 kDa decamer and 40 potential selenium sites. A four-wavelength MAD experiment, with data collected to 2.25 Å resolution at 100 K, was carried out. The positions of the selenium atoms were found automatically using CNS (Brünger *et al*., 1998) and CCP4 (CCP4, 1994), and maps of high quality were produced. The solvent-flattened map from DM (Cowtan, 1994) was used as input to the wARP procedure (Perrakis *et al*., 1999), which extended and improved phases and produced an initial protein model. The model was refined using *REFMAC* (CCP4, 1994) against data collected to a 1.65 Å resolution (*R*-factor = 15.2%, *R*-free = 19.0%). Structures of the enzyme complexed with chloride (cyanate analogue) and oxalate (proposed transition state analogue) were also determined (Walsh *et al*., 2000). These structures show that the active site of cyanase is formed by the side chains of four adjacent subunits of the homo-decamer.

We have further expanded experimental phasing by conducting MAD experiments at atomic resolution. A single crystal of aldose reductase substituted with SeMet was used to collect MAD data at atomic resolution (0.9 Å). These data provided a unique opportunity to compare the model refined at subatomic resolution with the experimental ‘unbiased’ electron density maps (Podjarny *et al*., 2003). The atomic model refined against subatomic-resolution data enables the determination with very high accuracy of the well ordered regions, and departures from the usual stereochemistry or unusually short contacts to be established. The unbiased experimental MAD maps can validate these unexpected structural features. It is also possible to determine fine details, like H atoms, in the well ordered regions. However, in the less-ordered regions, like side chains with multiple conformations or disordered solvent zones, the signal is weak for the low-occupancy conformers and it is necessary to validate possible interpretations. Brute-force refinement can lead to model bias, even at atomic resolution. It is in these regions where the experimental phases can be extremely useful, as they show clearly and unambiguously the multiple conformations. In the solvent zone, the experimental maps

indicate that only the water molecules with $B < 40$ Å^2 can be clearly assigned to an ordered site, while the remainder should only be considered as an indication of high-density values. Therefore the experimental phases from MAD experiments at atomic resolution can improve the interpretation of electron density maps and reduce the model bias in the less-ordered regions.

In the more general case, the prevalence of the MAD method in the solution of the phase problem has a strong impact on the speed and accuracy of obtaining a final model. In fact, since the MAD phases are free of model bias, interpretation of the electron density maps is more straightforward and can be automated leading in favorable cases to very fast structure determination (Walsh, Evans *et al*., 1999; Minor *et al*., 2005).

9. The SBC user program at beamline 19ID

The 19ID beamline was opened to outside users in 1998 and the general user program has been in operation since 1999. Currently the SBC operates a user program at sector 19 that is open to the crystallographic research community *via* a peer-reviewer proposal system operated by the APS user office. Users are scheduled three times a year; those who require immediate access can be scheduled during the current cycle if beam time is available. All projects are given beam time based upon the rating received when reviewed. There are two types of proposals: individual proposals, which are valid for one visit, and program proposals, which are valid for multiple visits over two years. At the present time, 75% of available beam time is allocated to the user program, 25% scheduled by the APS and 50% scheduled by SBC under its national user program mandate. Since beginning the user program in 1998, more than 1800 users, representing over 440 user groups, have collected data at the 19ID beamline of the SBC. These user groups used 19ID for determination of high-resolution structures of large macromolecular assemblies [examples include 50S ribosomal subunit, PDBIDs = 1S72/1XBP, 1.5 MDa/AU (Ban *et al*., 2000; Schluenzen *et al*., 2001); 30S ribosomal subunit, PDBIDs = 1I94/1IBK, 0.8 MDa/AU (Schluenzen *et al*., 2000; Ogle *et al*., 2001); GroEL/ES complex, PDBID = 1PCQ, 0.9 MDa/AU (Chaudhry *et al*., 2003)], several membrane proteins including outer-membrane transporter FecA (Ferguson *et al*., 2002), rhodopsin, a G protein-coupled receptor (Palczewski *et al*., 2000), membrane penetration protein from a non-enveloped virus (Dormitzer *et al*., 2004) and membrane-associated proteins such as integrin, an important surface receptor (Xiong *et al*., 2001), arrestin which binds to activated phosphorylated G protein-coupled receptors (Hirsch *et al*., 1999); important protein/nucleic acid complexes including Tn5 transposase complexed with Tn5 transposon end DNA (Davies *et al*., 2000), DNA polymerase holoenzyme/DNA complex (Murakami *et al*., 2002) and many others.

The 19ID productivity and quality of the data is also reflected in the number of peer-reviewed publications (currently 384) and journal covers for high-profile projects (currently 26). 19ID was the first undulator beamline designed for, and capable of, routine MAD/SAD experiments over a wide range of ‘absorption edges’ that covers *K*, L_{III} and *M* edges of the majority of elements used for phasing. It is a facility that established high-throughput approaches to structure determination using anomalous signal (MAD/SAD) (Walsh, Dementieva *et al*., 1999; Walsh, Evans *et al*., 1999). This is reflected also in the contribution of 19ID to the determination of novel structures and structural genomics programs in the USA (Fig. 8, Fig. 9). The brilliant beam of 19ID has produced very good data from very small crystals of (5–10 μm). Detailed information about the beamline, user program and applying for beam time can be found at the SBC web site, http://www.sbc.anl.gov.

In conclusion, over the past several years 19ID has met all design specifications and has become a significant resource for the macromolecular crystallography community. The beam-line is capable of data collection from crystals with very large unit cell, weakly diffracting crystals

and very small crystals. 19ID has strongly contributed to the broad application of anomalous signal for structure determination and to efficient data collection at atomic resolution. Moreover, 19ID is capable of high-throughput data collection and structure determination and its output can be compared with small synchrotron sources. 19ID has already made a major impact on structural biology.

We especially thank W. Minor (U. Virginia) and Z. Otwinowski (U. Texas) for their contribution to the final stages of SBC commissioning and making *HKL2000* available to us before its official release. In addition to the SBC staff coauthors of this paper, we acknowledge the efforts of R. Benn, M. Cuff, M. Ficner, Y. Kim, S. Korolev, J. Osipiuk and R. Schuessler in the continuing development and operation of the beamline 19ID and user program. This project is supported by the US Department of Energy, Office of Biological and Environmental Research, under contract W-31-109-Eng-38 and the NIH.

References

Alkire, RW.; Duke, NEC.; Rotella, FJ. Synchrotron Radiation Instrumentation: Eighth International Conference on Synchrotron Radiation Instrumentation, AIP Conference Proceedings. Warwick, T., et al., editors. 705. Melville, NY: American Institute of Physics; 2004. p. 827-830.

Alkire RW, Rosenbaum G, Evans G. J Synchrotron Rad 2000;7:61–68.

Alkire RW, Rotella FJ. J Appl Cryst 1997;30:327–332.

Alkire RW, Schuessler R, Rotella FJ, Gonczy JD, Rosenbaum G. J Appl Cryst 2004;37:836–840.

Ban N, Nissen P, Hansen J, Moore PB, Steitz TA. Science 2000;289:905–920. [PubMed: 10937989]

Brünger AT, Adams PD, Clore GM, DeLano WL, Gros P, Grosse-Kunstleve RW, Jiang JS, Kuszewski J, Nilges M, Pannu NS, Read RJ, Rice LM, Simonson T, Warren GL. Acta Cryst D 1998;54:905–921. [PubMed: 9757107]

Buttner, H., editor. ESRF Beamline Handbook. Grenoble; France: 1993. ESRF, BP 220, F-38043

Chaudhry C, Farr GW, Todd MJ, Rye HS, Brunger AT, Adams PD, Horwich AL, Sigler PB. EMBO J 2003;22:4877–4887. [PubMed: 14517228]

Clemons WM Jr, Brodersen DE, McCutcheon JP, May JL, Carter AP, Morgan-Warren RJ, Wimberly BT, Ramakrishnan V. J Mol Biol 2001;310:827–843. [PubMed: 11453691]

Collaborative Computational Project, Number 4. Acta Cryst D 1994;50:760–763. [PubMed: 15299374]

Cowtan K. Jnt CCP4 ESF-EACBM Newsl Protein Crystallogr 1994;31:34–38.

Darwin CG. Philos Mag 1914;27:315–333. 675–690.

Davies DR, Goryshin IY, Reznikoff WS, Rayment I. Science 2000;289:77–85. [PubMed: 10884228]

Dejus, RJ.; Vasserman, IB.; Sasaki, S.; Moog, ER. Technical Bulletin ANL/APS/TB-45. Argonne National Laboratory; Argonne, IL, USA: 2002.

Dormitzer PR, Nason EB, Prasad BV, Harrison SC. Nature (London) 2004;430:1053–1058. [PubMed: 15329727]

Ferguson AD, Charkraborty R, Smith BS, Esser L, Deisenhofer J. Science 2002;295:1715–1719. [PubMed: 11872840]

Garman E. Acta Cryst D 1999;55:1641–1653. [PubMed: 10531512]

Hendrickson WA. Trans Am Cryst Assoc 1985;21:11.

Hendrickson WA. Science 1991;254:51–58. [PubMed: 1925561]

Hirsch JA, Schubert C, Gurevich VV, Sigler PB. Cell 1999;97:257–269. [PubMed: 10219246]

Howard EI, Sanishvili R, Cachau RE, Mitschler A, Chevrier B, Barth P, Lamour V, Van Zandt M, Sibley E, Bon C, Moras D, Schneider TR, Joachimiak A, Podjarny A. Proteins 2004;55:792–804. [PubMed: 15146478]

Ilinski P, Dejus RJ, Gluskin E, Morrison TI. Proc SPIE 1996;2856:16–25.

Ivanov, I.; Rosenbaum, G.; Chrzas, J.; Fischetti, R.; Segre, CU.; Chapman, LD. Synchrotron Radiation Instrumentation Eleventh US National Conference, AIP Conference Proceedings 521. Pianetta, P.; Arthur, J.; Brennan, S., editors. New York: American Institute of Physics; 2000. p. 271-275.

Khounsary AM. Rev Sci Instrum 1992;63:461–464.

Knapp GS, Beno MA, Rogers CS, Wiley CL, Cowan PL. Rev Sci Instrum 1994;65:2792–2797.

Lazarski, KL.; Alkire, RW.; Duke, NEC.; Rotella, FJ. Eighth International Conference on Synchrotron Radiation Instrumentation (SRI2003), AIP Conference Proceedings. Warwick, T., et al., editors. 705. Melville, NY: American Institute of Physics; 2004. p. 612-615.San Francisco, CA, USA, 25–29 August 2003

Lazarski KL, Cymborowski M, Chruszcz M, Otwinowski O, Dauter Z, Minor W, Joachimiak A. 2006In preparation

Leslie AG. Acta Cryst D 1999;55:1696–702. [PubMed: 10531519]

Lima CD, D'Amico KL, Naday I, Rosenbaum G, Westbrook EM, Hendrickson WA. Structure 1997;5:763–774. [PubMed: 9261067]

McMaster, WH.; Kerr Del Grande, N.; Mallett, JH.; Hubbell, JH. Compilation of X-ray Cross Sections. Lawrence Livermore National Laboratory; USA: 1969. p. 27-30.UCRL-50174, Sec. II, Rev. 1

Matsushita, T.; Hashizume, H. Handbook on Synchrotron Radiation. Koch, E-E., editor. 1a. Amsterdam: North Holland; 1983. p. 267-274.

Minor, W.; Cymborowski, M.; Lazarski, L.; Chruszcz, M.; Otwinowski, O.; Joachimiak, A.; Dauter, Z. Meeting of the American Crystallographic Association; 2005. Abstract W0317

Moncton DE, Crosbie EN, Shenoy GK. Rev Sci Instrum 1989;60:1403–1405.

Murakami K, Masuda S, Campbell EA, Muzzin O, Darst SA. Science 2002;296:1285–1290. [PubMed: 12016307]

Nissen P, Hansen J, Ban N, Moore PB, Steitz TA. Science 2000;289:920–930. [PubMed: 10937990]

Ogle JM, Brodersen DE, Clemons WM Jr, Tarry MJ, Carter AP, Ramakrishnan V. Science 2001;292:897–902. [PubMed: 11340196]

Otwinowski Z, Minor W. Methods Enzymol 1997;276:307–326.

Palczewski K, Kumasaka T, Hori T, Behnke CA, Motoshima H, Fox BA, Le Trong I, Teller DC, Okada T, Stenkamp RE, Yamamoto M, Miyano M. Science 2000;289:739–745. [PubMed: 10926528]

Perrakis A, Morris R, Lamzin VS. Nature Struct Biol 1999;6:458–463. [PubMed: 10331874]

Pflugrath J. Acta Cryst D 1999;55:1718–1725. [PubMed: 10531521]

Podjarny A, Schneider TR, Cachau RE, Joachimiak A. Methods Enzymol 2003;374:321–341. [PubMed: 14696380]

Pohl E, Ristau U, Gehrmann T, Jahn D, Robrahn B, Malthan D, Dobler H, Hermes C. J Synchrotron Rad 2004;11:372–377.

Rogers CS, Mills DM, Fernandez PB, Knapp GS, Wulff M, Handfland M, Rossat M, Freund A, Marot G, Holmberg J, Yamaoka H. Rev Sci Instrum 1996:67.(CD-ROM)

Rosenbaum, G.; Fornek, T. Synchrotron Radiation Instrumentation Tenth US National Conference, AIP Conference Proceedings. Fontes, E., editor. 417. New York: American Institute of Physics; 1997. p. 178

Rosenbaum G, Rock L, Sullivan M, Khalid S. Nucl Instrum Methods Phys Res A 1988;266:475–478.

Rosenbaum G, Sullivan M, Fischetti R, Rock L. Rev Sci Instrum 1992;63:931.

Rosenbaum, G.; Westbrook, EM. Synchrotron Radiation Instrumentation Tenth US National Conference, AIP Conference Proceedings. Fontes, E., editor. 417. New York: American Institute of Physics; 1997a. p. 5

Rosenbaum, G.; Westbrook, EM. Synchrotron Radiation Instrumentation Tenth US National Conference, AIP Conference Proceedings. Fontes, E., editor. 417. New York: American Institute of Physics; 1997b. p. 186

Schluenzen F, Tocilj A, Zarivach R, Harms J, Gluehmann M, Janell D, Bashan A, Bartels H, Agmon I, Franceschi F, Yonath A. Cell 2000;102:615–623. [PubMed: 11007480]

Schlünzen F, Zarivach R, Harms J, Bashan A, Tocilj A, Albrecht R, Yonath A, Franceschi F. Nature (London) 2001;413:814–821. [PubMed: 11677599]

Sheldrick, GM. SHELX: Applications to Macromolecules. Dordecht: Kluwer; 1998.

Shu, D.; Preissner, C.; Nocher, D.; Han, Y.; Barraza, J.; Lee, P.; Lee, W-K.; Cai, Z.; Ginell, S.; Alkire, R.; Lazarski, K.; Schuessler, R.; Joachimiak, A. Proceedings of the Eighth International Conference

on Synchrotron Radiation Instrumentation (SRI2003), AIP Conference Proceedings. Warwick, T., et al., editors. 705. Melville, NY: American Institute of Physics; 2004. p. 1201-1204.San Francisco, CA, USA, 25–29 August 2003

Smither RK, Forster GA, Bilderback DH, Bedzyk M, Finkelstein K, Henderson CJ, White C, Berman LE, Stefan P, Oversluizen T. Rev Sci Instrum 1989;60:1486–1492.

Snell G, Cork C, Nordmeyer R, Cornell E, Meigs G, Yegian D, Jaklevic J, Jin J, Stevens RC, Earnest T. Structure 2004;12:537–545. [PubMed: 15062077]

Walsh MA, Dementieva I, Evans G, Sanishvili R, Joachimiak A. Acta Cryst D 1999;55:1168–1173. [PubMed: 10329779]

Walsh MA, Evans G, Sanishvili R, Dementieva I, Joachimiak A. Acta Cryst D 1999;55:1726–1732. [PubMed: 10531522]

Walsh MA, Otwinowski Z, Perrakis A, Anderson PM, Joachimiak A. Structure Fold Des 2000;8:505–14. [PubMed: 10801492]

Weeks CM, Miller R. J Appl Cryst 1999;32:120–124.

Westbrook EM, Naday I. Methods Enzymol 1997;276:44–68.

Williams WA, Zhang RG, Zhou M, Joachimiak G, Gornicki P, Missiakas D, Joachimiak A. Biochemistry 2004;43:16193–16202. [PubMed: 15610013]

Wimberly BT, Brodersen DE, Clemons WM Jr, Morgan-Warren RJ, Carter AP, Vonrhein C, Hartsch T, Ramakrishnan V. Nature (London) 2000;407:327–339. [PubMed: 11014182]

Xiong JP, Stehle T, Diefenbach B, Zhang R, Dunker R, Scott DL, Joachimiak A, Goodman SL, Arnaout MA. Science 2001;294:339–345. [PubMed: 11546839]

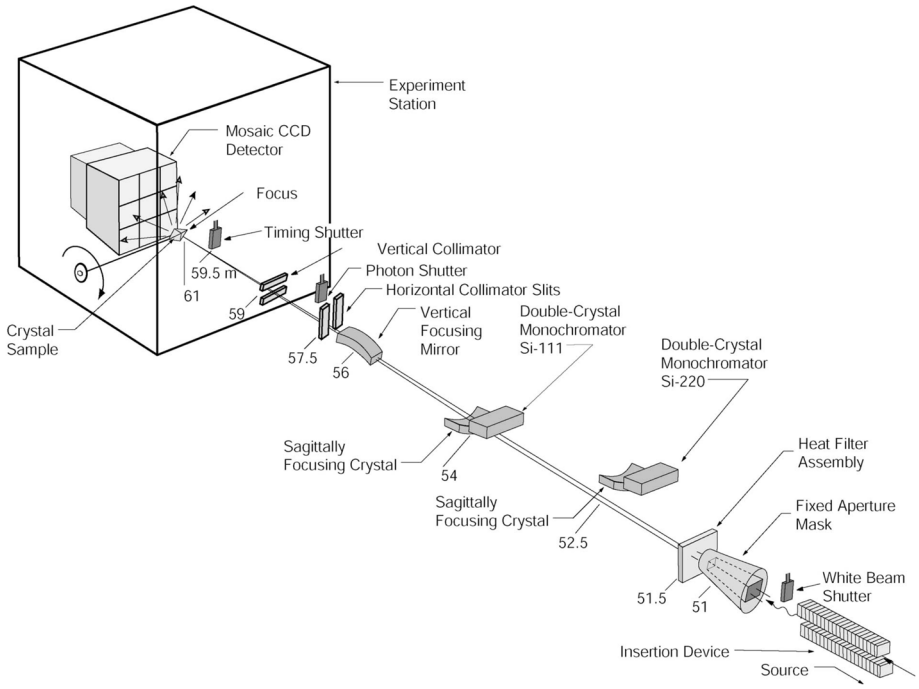

Figure 1.

Schematic diagram showing the relative location of the optical components in 19ID. [Indicated distances are from the center of the straight section, not from the center of the radiation source (undulator) as in the text.]

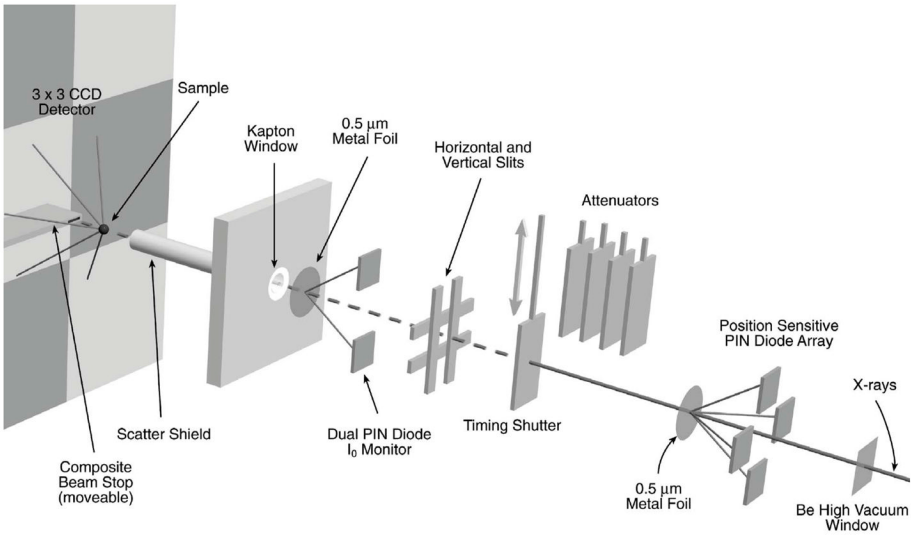

Figure 2.
Schematic diagram of the endstation components, including X-ray beam-position monitors, timing shutter, attenuators, beam stop, sample and CCD detector.

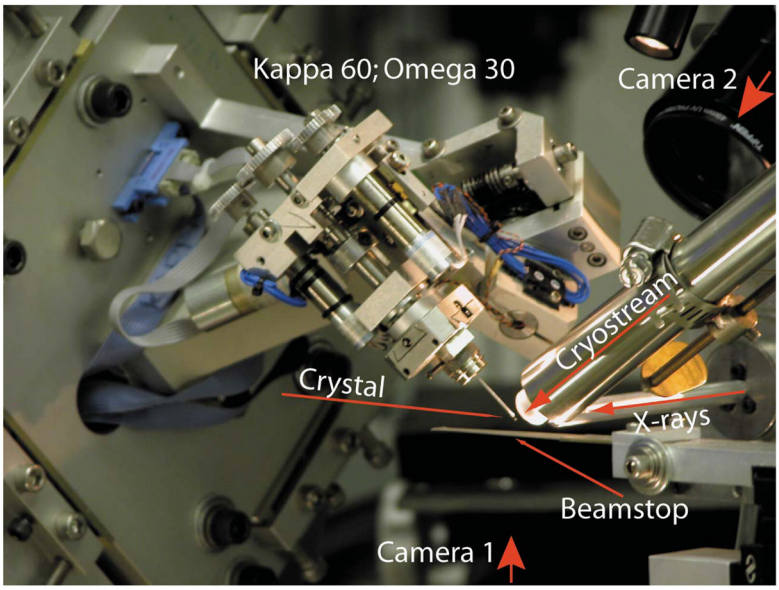

Figure 3.
Photograph of the sample area showing the κ goniometer (center), beam stop (left of sample), sample cooler (center right), objective lens of the alignment microscope and output of fiber-optic lighting (top right). The beam comes from the right through the beam transport tube (right center; scatter guard plug not visible).

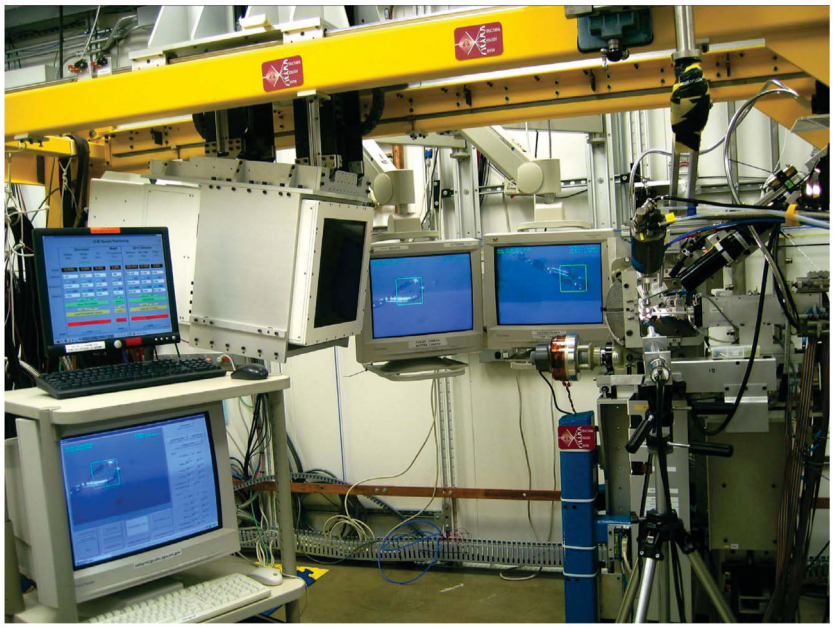

Figure 4.
Detector support with the ADSC Quantum 315 detector moved back for free access to the goniometer, displays of alignment cameras (center back), local beamline control terminal (left), goniometer with cameras and cold stream (right) and fluorescence detector (right foreground). The beam direction is from right to left.

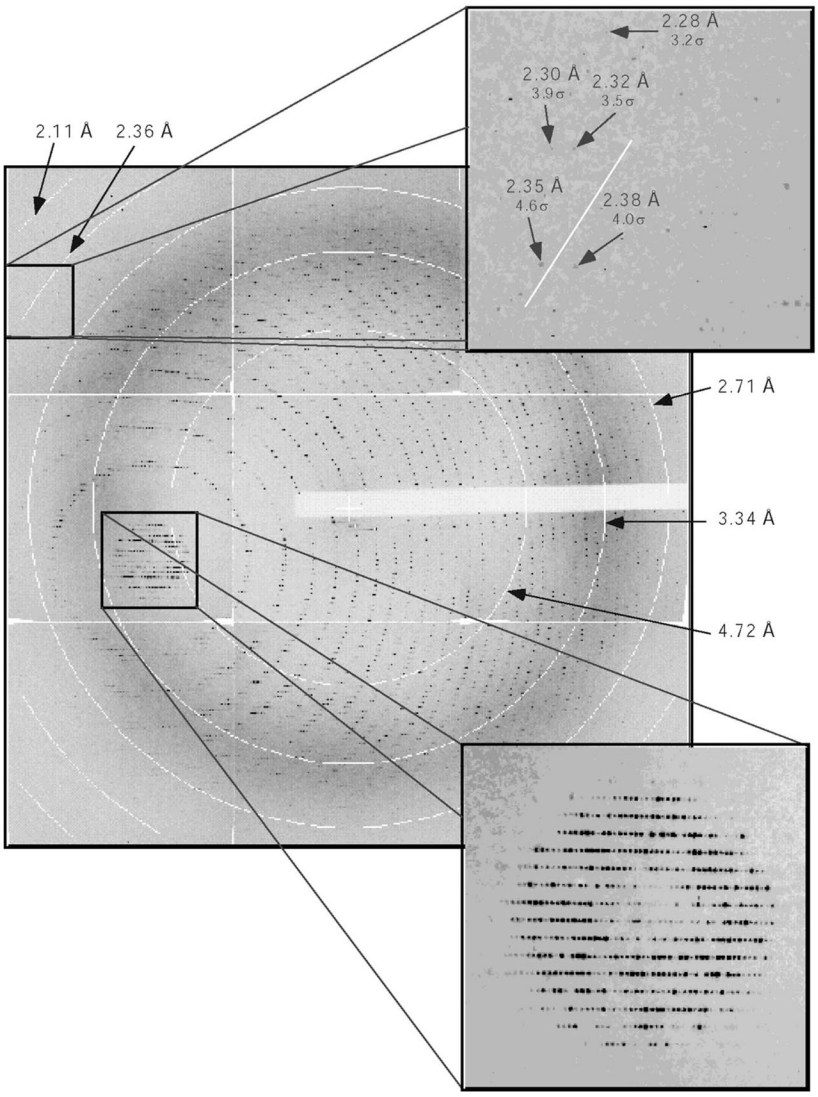

Figure 5.
Resolving power of the mosaic 3 × 3 CCD detector SBC2 demonstrated by the recording of a diffraction pattern from the 50S ribosomal subunit (orthorhombic space group $C222_1$, a = 212, b = 301, c = 576 Å). Resolution markers (circles), the resolution limit (upper enlargement) and the spatial resolution (lower enlargement) of the measurement are shown. (Courtesy of Dr T. Steitz, Yale University.)

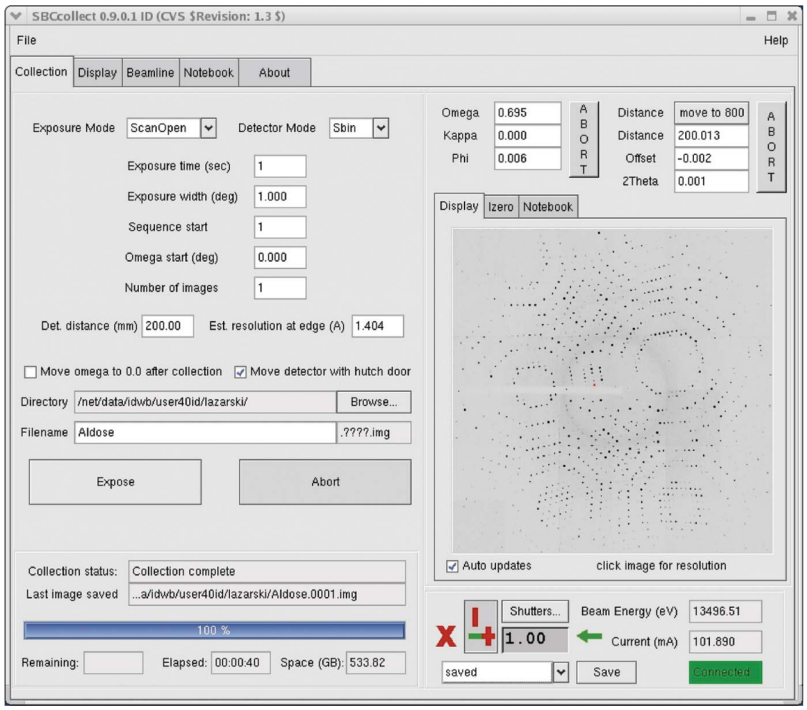

Figure 6.
Screen shot of the *SBCcollect* graphical user interface.

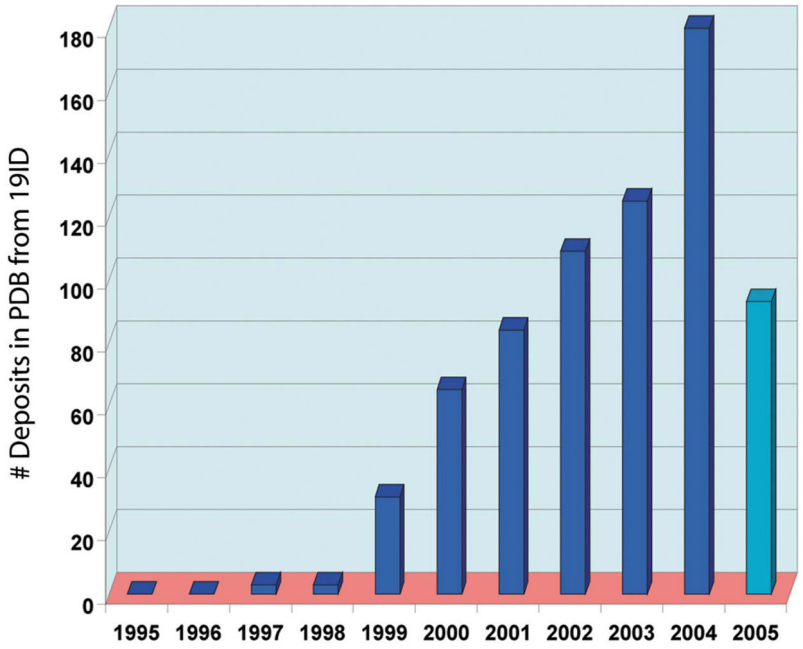

Figure 7.
Statistics of the Protein Data Bank structure depositions using data collected at beamline 19ID plotted versus year of deposition. (For 2005, data are incomplete.)

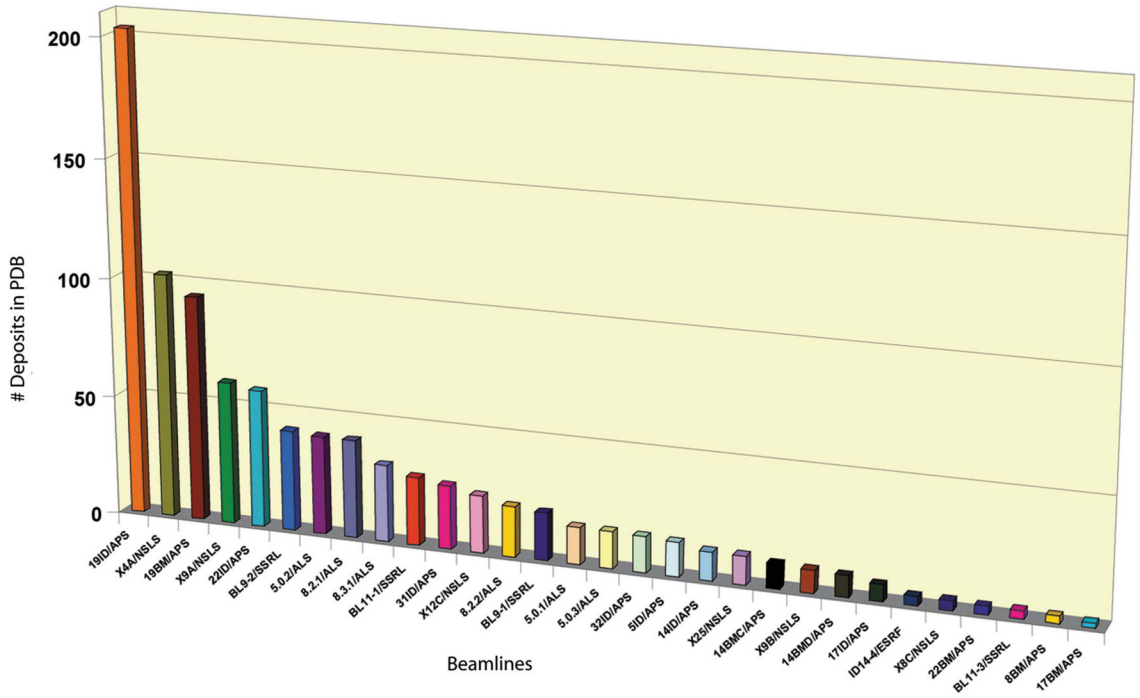

Figure 8.
Contributions of the Protein Data Bank deposits to the Protein Structure Initiative program by US synchrotron beamlines.

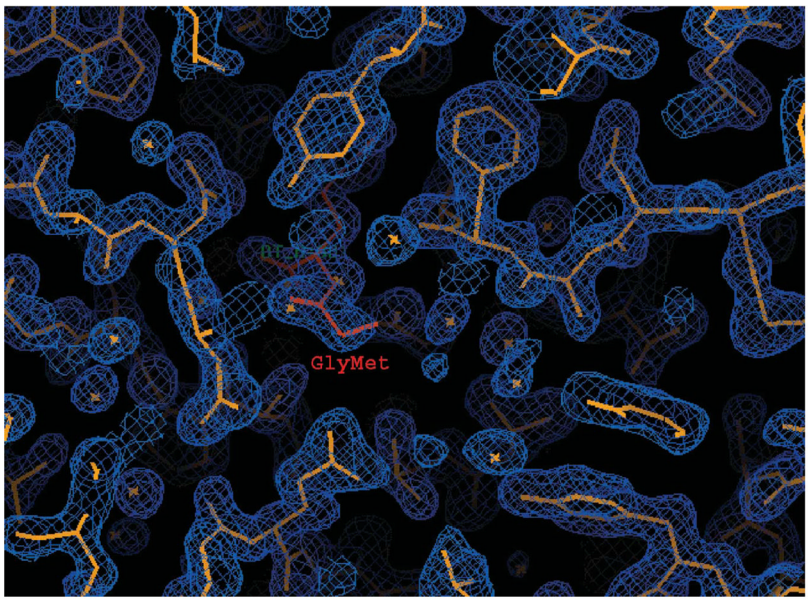

Figure 9.
1.7 Å SAD map of membrane-associated lipoprotein-9 GmpC from *Staphylococcus aureus* contoured at 1σ. A single Se atom was used to phase the 297 residues protein (Williams *et al*., 2004).

Table 1

Beamline performance measured during commissioning of 19ID.

Parameter	Measured performance
Photon energy (Si 111 monochromator crystals)	5–20 keV
Energy resolution ($\Delta E/E$)	1.41×10^{-4} FWHM
Harmonic contamination	<0.036%
Rate of energy change at 12 keV	1250 eV s^{-1}
Focus size	
Vertical	0.020 mm FWHM
Horizontal	0.083 mm FWHM
Maximum accepted divergence from source at 12 keV	
Vertical	0.04 mrad
Horizontal	0.08 mrad
Beam position stability at focus	<0.010 mm
Specimen-to-detector distance	100–1500 mm
Flux (Si 111 monochromator crystal, first undulator harmonic at 12 keV)	1.3×10^{13} photons s^{-1} $(100\ mA)^{-1}$
Flux density at focus in fully focused beam	3.6×10^{15} photons s^{-1} mm^{-2}
Efficiency of beamline (ratio of measured to calculated flux)	80%

Table 2

Aldose reductose: statistics of the 0.66 Å native data collection as a function of resolution range (Howard *et al.*, 2004). *R-mer* compares reflections from different scans.

Shell limit (Å)								
Lower	**Upper**	**Completeness (%)**	**Average *I***	**Average error**	**Average statistical error**	**Normalized χ^2**	**Linear *R-mer***	**Square *R-mer***
20.00	1.79	99.2	175515.9	9343.2	3832.9	1.028	0.022	0.024
1.79	1.42	99.6	31861.7	2368.0	932.6	1.026	0.032	0.033
1.42	1.24	99.8	17021.0	1377.2	492.6	1.023	0.035	0.036
1.24	1.13	99.8	13442.3	1178.0	418.6	1.025	0.038	0.039
1.13	1.05	99.6	8930.7	791.5	288.4	1.019	0.041	0.041
1.05	0.99	98.9	5236.5	454.5	187.9	1.025	0.045	0.045
0.99	0.94	96.6	3417.6	321.9	166.2	1.024	0.053	0.052
0.94	0.90	94.4	2496.1	246.8	150.8	1.022	0.060	0.059
0.90	0.86	92.3	1831.8	190.9	128.8	1.029	0.067	0.065
0.86	0.83	90.1	1453.7	168.2	123.8	1.024	0.079	0.076
0.83	0.81	88.4	1186.4	149.5	117.2	1.025	0.089	0.084
0.81	0.78	86.6	1027.2	141.4	119.2	1.023	0.099	0.094
0.78	0.76	84.9	920.0	141.2	122.7	1.028	0.110	0.105
0.76	0.74	83.3	820.7	142.8	127.1	1.027	0.126	0.119
0.74	0.73	81.8	706.1	142.0	128.9	1.025	0.144	0.135
0.73	0.71	80.1	621.2	140.7	131.0	1.029	0.161	0.151
0.71	0.70	78.5	523.5	140.5	132.2	1.029	0.191	0.179
0.70	0.68	77.5	446.1	139.6	135.1	1.028	0.220	0.206
0.68	0.67	76.0	371.9	139.8	139.0	1.020	0.260	0.238
0.67	0.66	74.7	317.3	142.9	142.9	0.990	0.301	0.280
All reflections		89.1	14989.8	985.9	434.7	1.024	0.029	0.024